-Supporting Information-

Tailoring Electronic Structures of Ni@N-doped Carbon Hollow Urchins for Dual-Functional Zn-CO_2 Batteries and Industrial CO_2 Electroreduction

Songjiang Wu[a, c+], Di Wang[b+], Haijian Wang[c], Haiyan Chen[c], Shenjie Yu[c], Xinyu Zhuang[b], Hao Zhang[d*], Suqin Ci[a*], Zhenhai Wen[b, c*]

Experimental

Materials

All reagents and chemicals were procured from commercial sources and utilized without additional purification. Nickel nitrate ($Ni(NO_3)_2 \cdot 6H_2O$), KOH (90 wt%), trimesic acid (H_3BTC), Polyvinylpyrrolidone (PVP, Mw = 40000), dicyandiamide (DCDA), ethanol, and N, N-dimethylformamide (DMF) were procured from Sinopharm Group Chemical Reagent Co. Ltd. Nafion solution (5 wt%) was obtained from DuPont.

Preparation of Ni@N-HCS-X

The synthesis process of the material involved the preparation of Ni-MOF@DCDA followed by pyrolysis to obtain Ni@N-HCS-X. To prepare Ni-MOF@DCDA, a mixture was prepared by dissolving $Ni(NO_3)_2 \cdot 6H_2O$ (0.864 g), H_3BTC (0.3 g), and PVP (3.0 g) in 60 ml of a mixed solution of distilled water, ethanol, and DMF in a ratio of 1:1:1 (v/v/v). The solution was vigorously stirred, and then DCDA (4.204 g) was added. The resulting mixture was further stirred for 1 h at room temperature (RT). The light green solution was transferred to a 100 ml Teflon-lined autoclave and heated at 150 °C for 10 h. The final product was collected through centrifugation, washed with ethanol three times, and dried in a vacuum oven at 60 °C for 12 h, resulting in Ni-MOF@DCDA. Next, the obtained Ni-MOF@DCDA powder was placed in a tube furnace and subjected to pyrolysis. The sample was heated under an argon atmosphere at a specific temperature (X=700, 800, or 900 °C) for 2 h, with a heating rate of 5 °C min^{-1}. Subsequently, the powder was naturally cooled to room temperature. The pyrolyzed powder was then stirred in 1 M hydrochloric acid for 12 h to obtain Ni@N-HCS-X.

Preparation of Ni-MOF-X and Ni@HCS-X

The control samples of Ni@C-800 and Ni@HCS-800 were also prepared, except

without the addition of DCDA and PVP, respectively.

Methods

Material characterizations

X-ray diffraction (XRD) patterns were obtained via the use of an X-ray diffractometer (D8 Advance, Bruker, Germany) equipped with Cu-Kα radiation (λ= 0.15406 nm). Raman spectra were acquired via the use of a LabRAM HR instrument. The ATR-IR spectra were captured using a Nicolet iS50 FT-IR spectrometer equipped with an MCT detector. X-ray photoelectron spectra (XPS) results were acquired using an ESCALAB 250Xi XPS spectrometer (Thermo Scientific) with an Al Kα excitation source (1486.6 eV). Scanning electron microscope (SEM) patterns were recorded using a SU-8010 instrument, while transmission electron microscope (TEM) patterns were captured using a Tecnai F20 instrument.

Electrochemical measurement

To prepare the catalyst ink, 5 mg of the sample was dispersed ultrasonically in a solution (500 μL) containing Nafion (50 μL), ethanol (350 μL), and water (100 μL) for a duration of 30 min. Subsequently, 100 μL of the catalyst ink was dropwise pipetted onto a carbon paper substrate and dried. The catalyst loading of the electrode was 1 mg cm^{-2}.

Electrochemical measurements were conducted using a CHI 660E electrochemical workstation, utilizing a standard three-electrode configuration. All potentials were referenced to the reversible hydrogen electrode (RHE), and conversion was performed using the following formula: $E_{RHE} = E_{Ag/AgCl} + 0.197 + 0.059 \times pH$. It is crucial to highlight that no internal resistance (iR) compensation was applied during the electrochemical measurements.

All electrochemical tests were conducted using an H-cell configuration, with a Nafion 117 membrane separating the compartments. The counter electrode consisted of a

platinum mesh (1 × 1 cm^2), while an Ag/AgCl electrode (saturated KCl) served as the reference electrode. The working electrode employed a carbon paper (1 × 1 cm^2) supporting our sample. The electrocatalytic reduction of CO_2 was carried out in a 0.5 M $KHCO_3$ electrolyte. Prior to each CO_2RR test, the electrolyte was saturated with CO_2 for a minimum of 30 min, with a consistent flow rate of 20 cm^3 min^{-1} maintained throughout the experiments. For the flow-cell test, the gas diffusion electrode (GDE) of the cathode was prepared by carefully drop-coating 1.0 mg cm^{-2} catalyst onto a 1 × 1 cm^2 carbon paper in CO_2-saturated 3 M KCl electrolytes. In the anodic chamber, a piece of Ni foam was employed as the anode in 1 M KOH electrolytes. Both the catholyte and anolyte were continuously circulated through their respective chambers using a peristaltic pump.

The cathode of a homemade Zn-CO_2 flow battery was prepared by coating Ni@N-HCS-800 catalyst onto carbon paper, achieving a loading density of 1.0 mg cm^{-2}. For the anode, we utilized polished Zn flakes. The electrolyte compositions were as follows: a mixture of 6 M KOH and 0.2 M zinc acetate served as the anode electrolyte, while 1 M $KHCO_3$ was employed as the cathode electrolyte. The bipolar membrane effectively separated the two compartments. A controlled flow rate of 20 cm^3 min^{-1} CO_2 was continuously pumped into the cathode electrolyte throughout the experiment. Discharge polarization curves were obtained by performing linear sweep voltammetry (LSV) with a scan rate of 5 mV s^{-1}. Additionally, chronopotentiometry was utilized to capture charge and discharge curves at a fixed current density of 2 mA cm^{-2}, with each 20-minute cycle comprising 10 min of charging and 10 min of discharging.

For continuous analysis of the gas products, the cathode chamber was connected to an online gas chromatograph (GC9860) equipped with a PQ column and a TCD detector. The Faraday efficiency of the gas products was determined using the following formula:

$$FE = \frac{e_{output}}{e_{input}} \times 100\% = \frac{N_{(CO/H_2)} \times n \times F}{I \times t} \quad (1)$$

$$t = \frac{60 \times v}{r} \text{ Second} \quad (2)$$

Where FE is the Faraday efficiency of a certain product, e_{input} and e_{output} are the total charge provided and the charge used for the reduction of a certain product, respectively. $N_{(CO/H2)}$ is the number of moles of product CO or H_2 (measured by GC), n is the number of electrons transferred to produce 1 mol of product, and 2 is for CO and H_2. F is the Faraday constant (96485 C mol^{-1}), I is the test current density, t is the time for the sample to fill the loop, v is the volume of the loop, and r is the CO_2 flow rate.

Computational Methods

DFT parameters

All the calculations are implemented by the PWSCF codes contained in the Quantum ESPRESSO distribution [1]. Spin-polarized DFT calculations were performed with periodic super-cells under the generalized gradient approximation (GGA) using the Perdew-Burke-Ernzerhof (PBE) functional for exchange-correlation and the ultrasoft pseudopotentials for nuclei and core electrons. The Kohn-Sham orbitals were expanded in a plane-wave basis set with a kinetic energy cutoff of 30 Ry and a charge-density cutoff of 300 Ry. The Fermi-surface effects have been treated by the smearing technique of Methfessel and Paxton, using a smearing parameter of 0.02 Ry. Periodical supercells containing single-layer graphene with 15 Å vacuum above were used to model various graphene doping structures. To model the doping N in the basal plane, we used the supercell of lateral size 4 × 4. For the doping N in the edge, we used the supercell of lateral size 3 × 5. We added 8 metal-cluster atoms of nickel underneath these active sites of graphitic carbon to simulate the graphene-covered metal cluster structure. For Ni (111), a 1×1 supercell and an eight-layer slab are utilized. The bottom four layers are fixed to model Ni bulk. The Brillouin zone was sampled with (1 × 1 ×

1) Monkhorst–Pack k-points.

Virtual energetic span as the activity-determining term

Norskov's approach uses the largest Gibbs energy (ΔGmax) as the activity-determining term. This descriptor is proposed under the assumption of the so-called "rate-determining step assumption": the slowest step should control the total kinetics of a series process [2]. However, for a multi-step reaction that takes place at a limited position, such as a catalytic reaction, it has been gradually noticed in the last ten years that there is no such thing as a "rate determining step" (RDS), instead, there should be a "rate determining state" [3]. That is, the catalytic activity should be co-determined by several steps. Based on such an idea, one should avoid using $\Delta G^{\max}$, but build a newly proposed descriptor that abandons the use of RDS. There are now two such kinds of descriptors, one is the highest free energy of a reaction intermediate (denoted as $G_{\max}$(RI)), proposed by Exner *et al.* [4]. The other is the "virtual energetic span" (δE^{v}) proposed by us. [5] And we will use the latter as the activity determining term in this paper.

The "virtual energetic span" (δE^{v}) comes from the "energetic span" proposed by Kozuch *et al.* [6]. It is the simplification of the result of a full microkinetic model. We won't go into too much detail here because it has given detailed illustrations in the ref. [5]. Here, we only give its brief conclusion: to use the virtual energetic span, we can still follow the basic principle of Norskov's method to build a *TS*-free FED. What is different from Norskov's approach is that we can treat the mid-point of each joint line in FED as the "virtual transition states (*TS*v)". We name it a virtual transition state because it is not the real energy of the transition state, but it has a constant difference from the real energy of the transition state. This can be strictly proved under the method of Norskov. Among those TS^{v}, there is one that determines the turnover frequency (TOF), which we name the TOF-determining TS^{v}, aliased as $TDTS^{v}$. On the other hand, for the energies of the intermediates, that is, the energy levels of the steps in FED, there is also one step that determines the activity. It is named the TOF determining

intermediate (*TDI*). The δE^v is calculated simply by the difference between $TDTS^v$ and *TDI*:

$$\delta E^v = TDTS^v - TDI \quad \text{(S1)}$$

When obtaining the δE^v, the TOF can be simply calculated by

$$TOF = k_0 exp(-\delta E^v/RT) \quad \text{(S2)}$$

The result should be the same as that deduced from a complete microkinetic model. So, the only question left would be the definitions of $TDTS^v$ and *TDI*. We can collect all the energy of the intermediates, [7] and all the energies of the TS^v $\{TS^v_i\}$. Then we pick one TS^v_i and one $\{I_i\}$. The difference between them should form a new set: $\{TS^v_i - I_j\}$. In this set, we add an element ΔG^r_{ij}, which will lead the general term formula of the set to be: $\{TS^v_i - I_j + \Delta G^r_{ij}\}$, where ΔG^r_{ij} is expressed as:

$$\Delta G^r_{ij} = \begin{cases} n\eta e & if\ \ i < j\ (means\ I_j\ locates\ after\ TS_i{}^v) \\ 0 & if\ i > j\ (means\ I_j\ locates\ before\ TS_i{}^v) \end{cases} \quad \text{(S3)}$$

With n and η, the total electron transfer number and the applied overpotential. $TDTS^v$ and *TDI* are then the $TS^v_i - I_j$ that will maximize $\{TS^v_i - I_j + \Delta G^r_{ij}\}$.

A brief introduction to the computational hydrogen electrode (CHE) method

When studying the electrocatalytic reaction through first principles, there are two difficulties: one is to calculate the reaction barrier of the proton-coupled electron transfer (PCET) reaction, the other is the Gibbs free energy of the solvated H^+. The CHE method [8] proposed by Norskov et al aims at settling or bypassing these two difficulties. In the framework of the CHE method, for the reaction

$$H^+ + e \rightarrow 1/2H_2 \quad \text{(S4)}$$

reaches equilibrium on U_{SHE}=0 V, one can replace the energy of H^+ with that of $1/2H_2$:

$$G_{H^+} = 1/2G_{H2} \quad \text{(S5)}$$

The energy of an electron can be expressed by –Ue, where *U* is the electrode potential vs SHE. As for the reaction barrier of PCET, the CHE method assumes the overpotential of the electrocatalytic reaction is the overpotential least required to make

standard reaction Gibbs free energies of all the elementary steps exothermic. And such potential is called the reaction limiting potential, which is denoted as U_l. Usually, U_l is an activity descriptor; as for CO_2RR, U_l can be used to judge the exact reaction pathway.

The reaction models and pathway

The reaction mechanisms for CO_2RR are written as follows:

$$CO_2+H^++e+*\rightarrow COOH* \quad \text{(S6)}$$

$$COOH*+H^++e\rightarrow CO*+H_2O(l) \quad \text{(S7)}$$

$$CO* \rightarrow CO(g)+* \quad \text{(S8)}$$

The asterisk stands for the sites on the surface of the catalysts.

In calculating the Gibbs free energy differences from R4 to R12, the associated adsorption free energy of the adsorbates is calculated by the following expression:

$$G_A = E_A + ZPE - TS + \int C_p dT \quad \text{(S9)}$$

Where E_A is the total energy of a certain molecule or adsorbate A*. When A represents a certain molecule, the total energies can be calculated directly. When A is representing a certain adsorbate, it is calculated by the difference between the DFT-based substrate with (E_{A*}^{DFT}) and without adsorbate A (E_*^{DFT}):

$$E_A = E_{A*}^{DFT} - E_*^{DFT} \quad \text{(S10)}$$

ZPE, TS and $\int C_p dT$ are the corrections from zero point energy, entropy and heat capacity, whose values are listed in Table S5. Other than that, H^+ is calculated by the Gibbs free energy of $1/2H_2$, and the energy of the electron is calculated by $-Ue$. A correction of -0.51 eV is added to CO molecules for the errors of the GGA-PBE functional. According to Ref. [9]. such a correction can lead to an agreement with the experimental overall half reaction of CO_2 reduction.

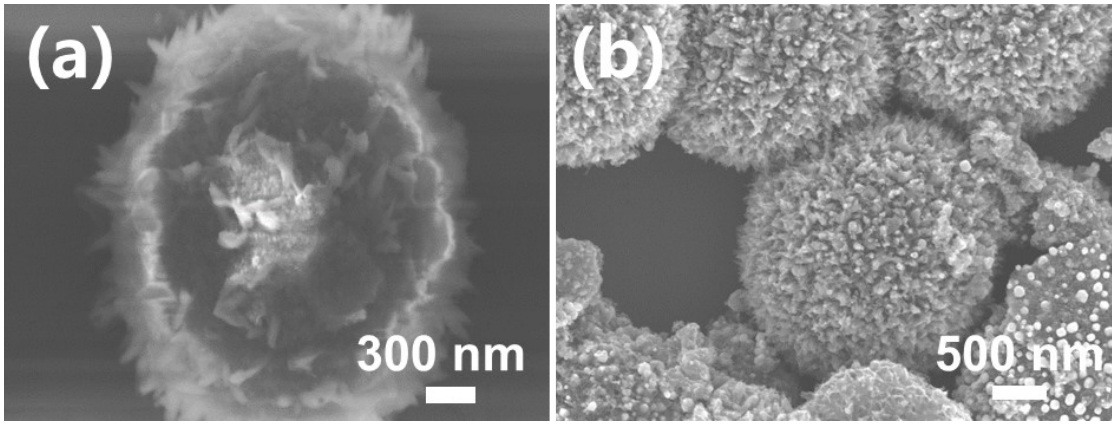

Figure S1. SEM images of (a) Ni-MOF, and (b) Ni@N-HCS-800 before acid etch.

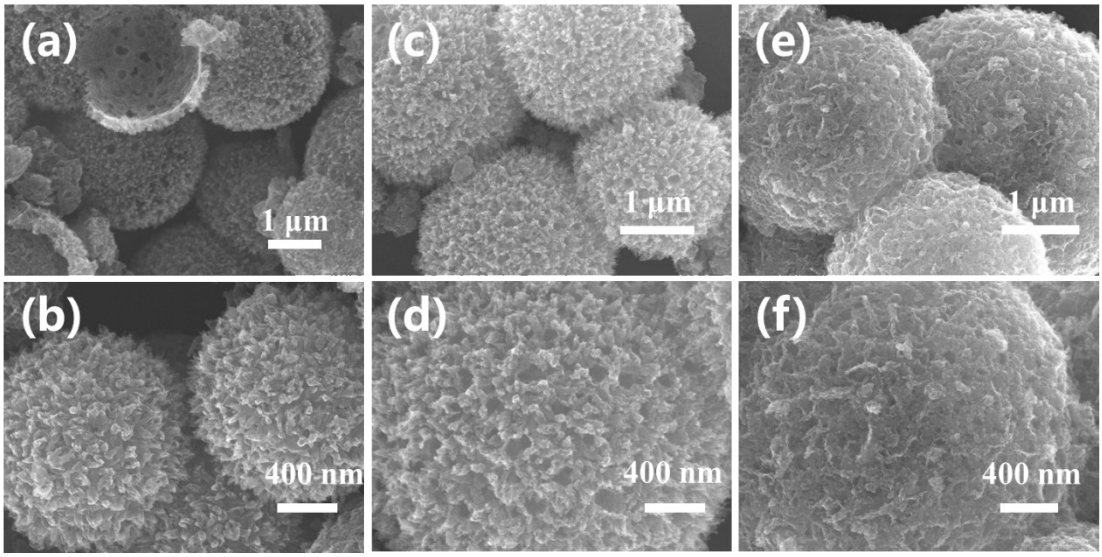

Figure S2. SEM images of (a-b) Ni@N-HCS-700, (c-d) Ni@N-HCS-800, (e-f) Ni@N-HCS-900.

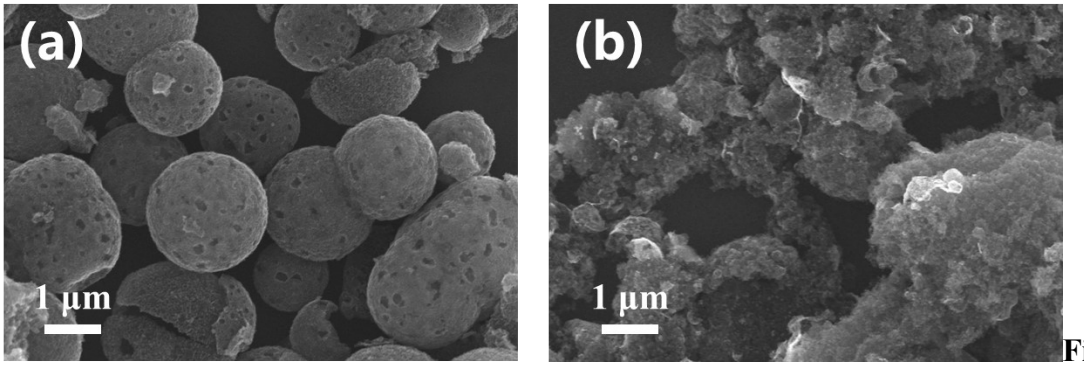

Figure S3. SEM images of (a) Ni@C-800 and (b)Ni@HCS-800.

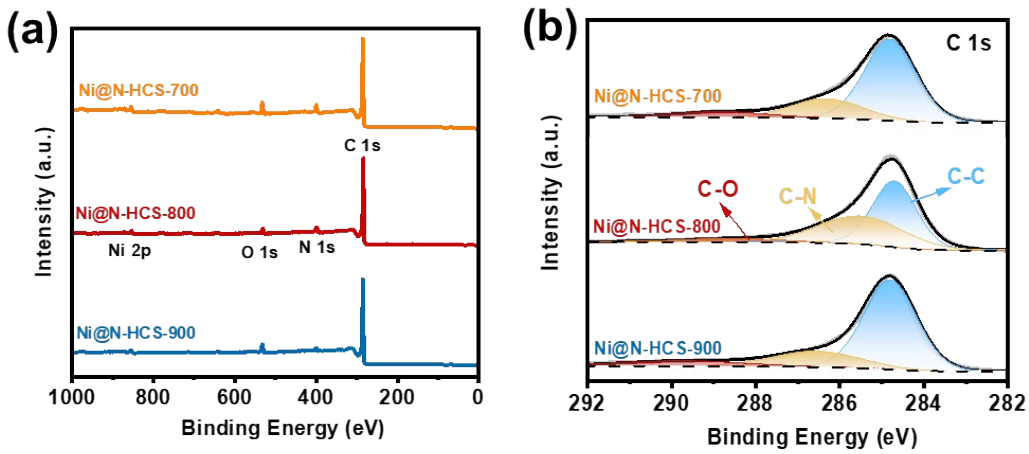

Figure S4. (a) XPS surveys and (b) C 1s spectra of Ni@N-HCS-700, Ni@N-HCS-800 and Ni@N-HCS-900.

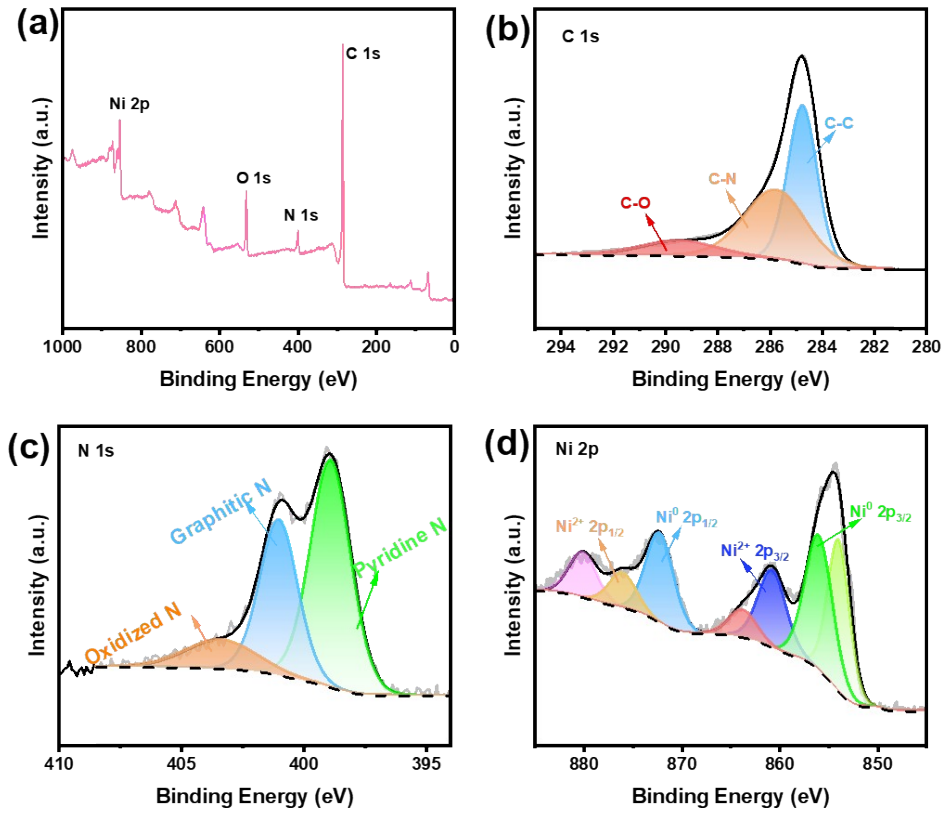

Figure S5. XPS analysis of Ni@N-HCS-800 before acid etch.

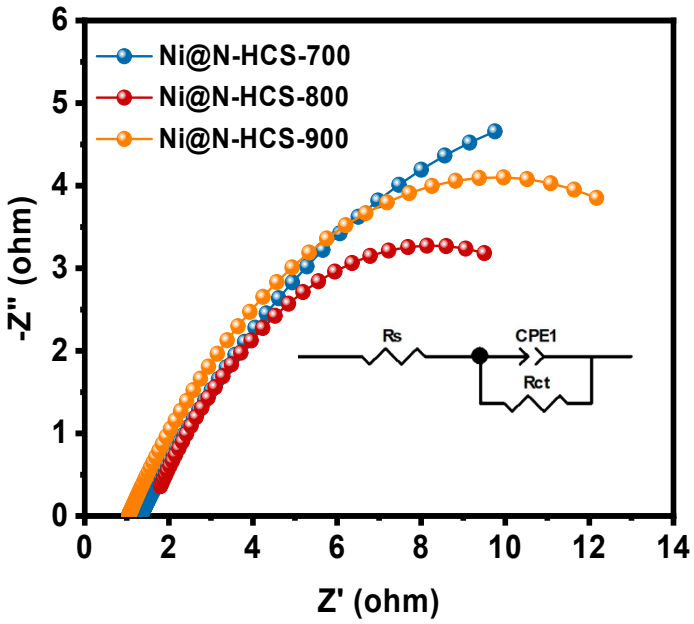

Figure S6. Nyquist plots for different catalysts.

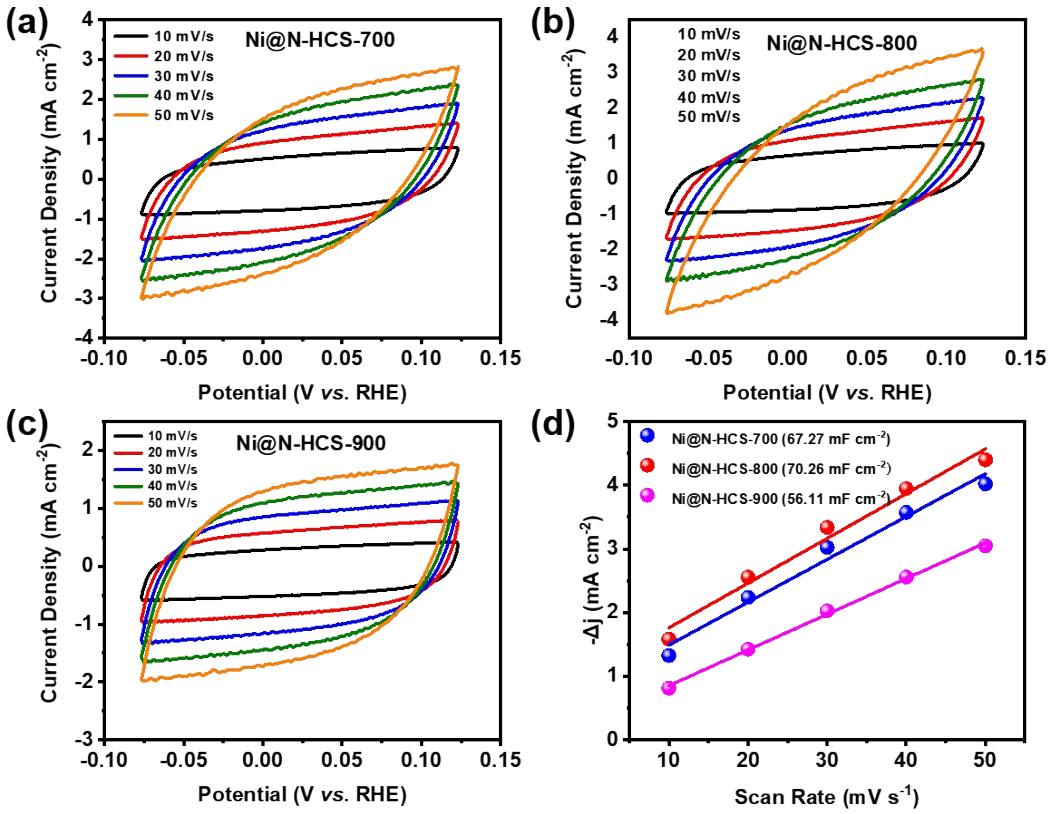

Figure S7. (a-c) CV curves at different scan rates. (d) The double-layer capacitance (Cdl) of different samples.

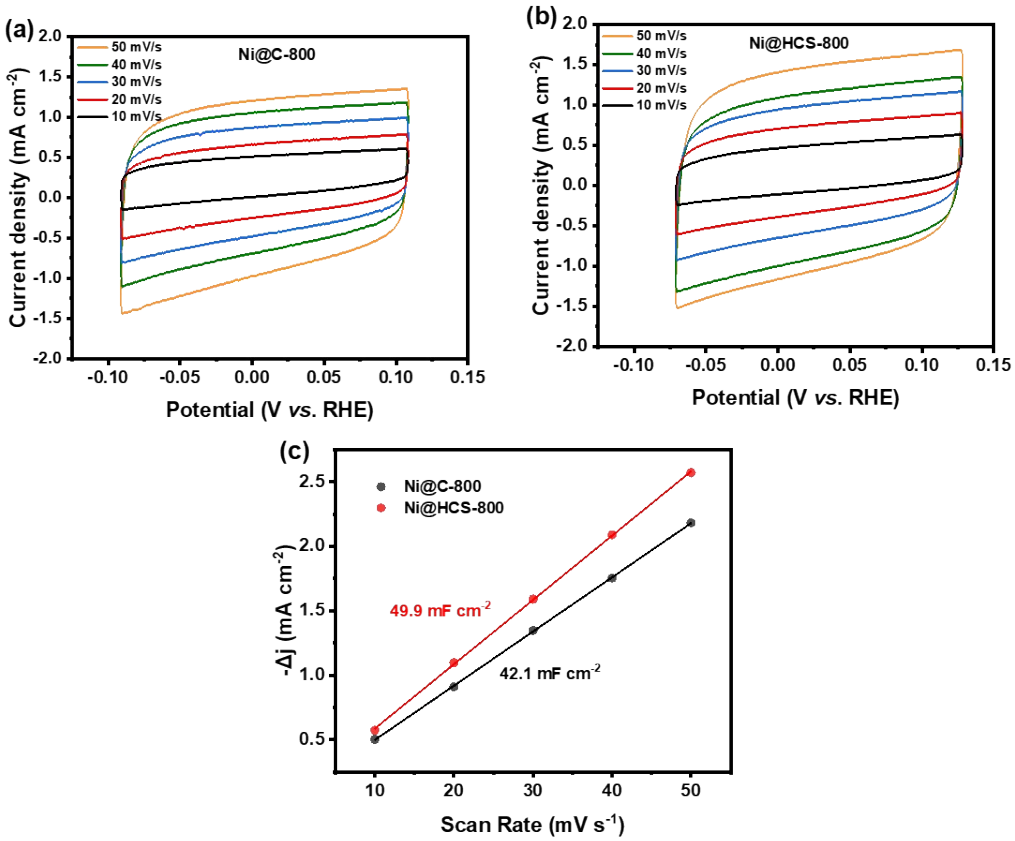

Figure S8. (a-b) CV curves at different scan rates and (c) the double-layer capacitance (Cdl) of Ni-MOF-800 and Ni@HCS-800.

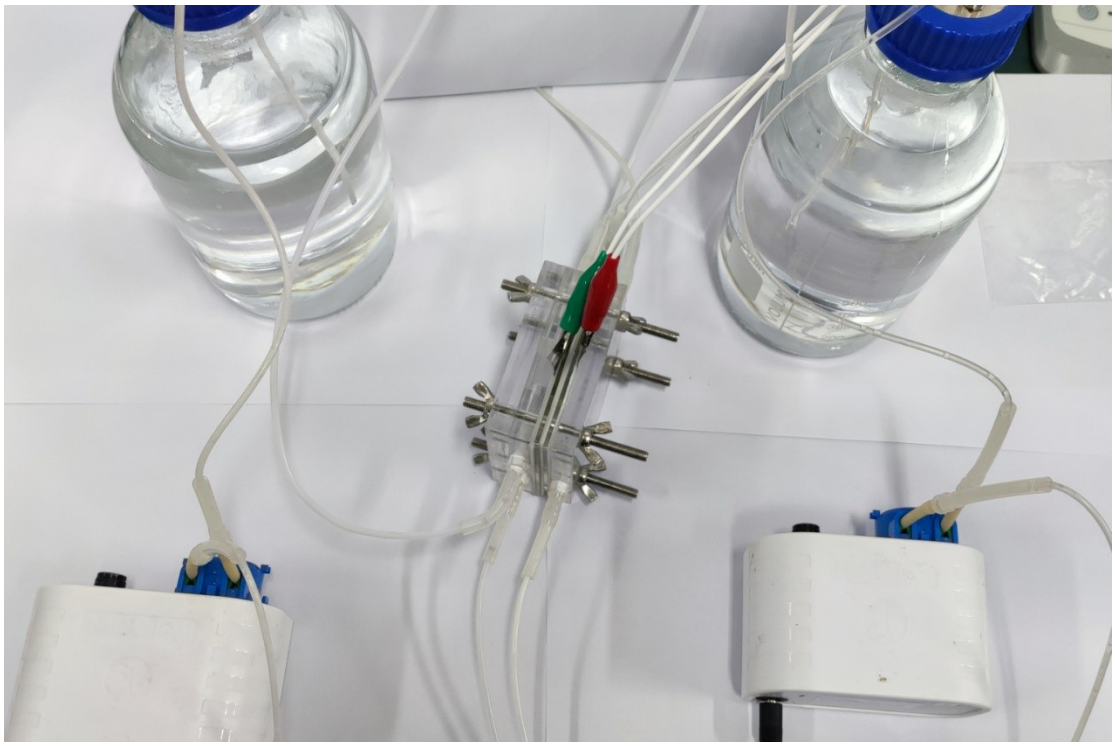

Figure S9. The photograph of flow cell.

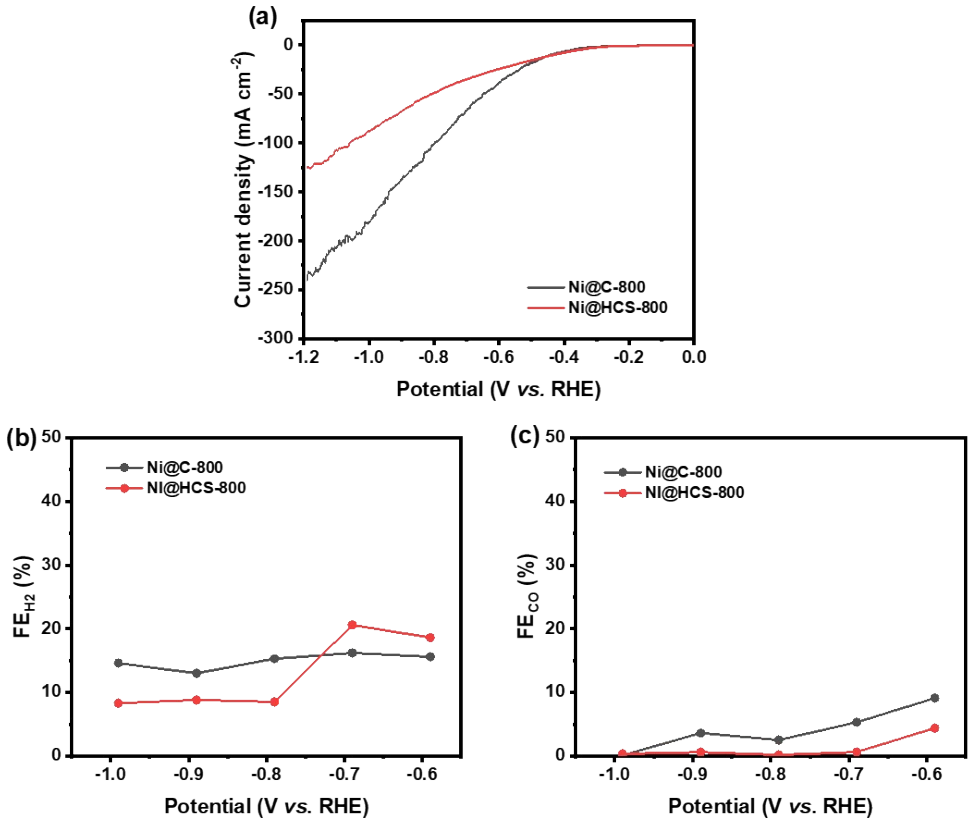

Figure S10. Electrocatalytic CO_2RR performance of Ni@C-800 and Ni@HCS-800. (a) LSV curves, (b) CO Faradic Efficiency (FE_{CO}) and (c) H_2 Faradic Efficiency (FE_{H2}).

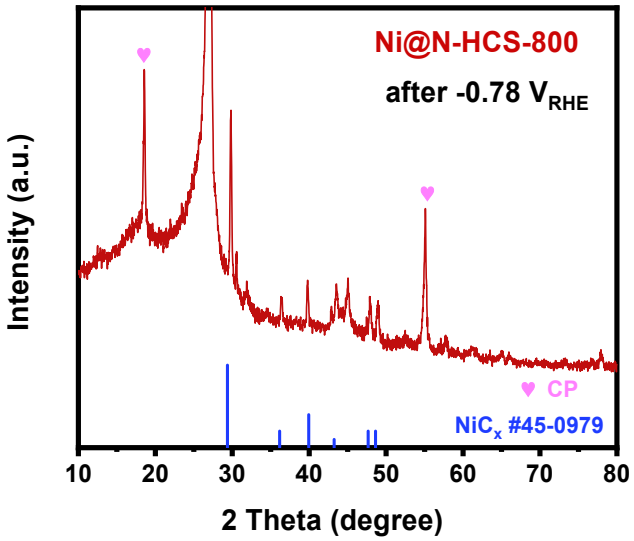

Figure S11. XRD pattern of Ni@N-HCS-800 after CO_2RR at -0.78 V for 1h.

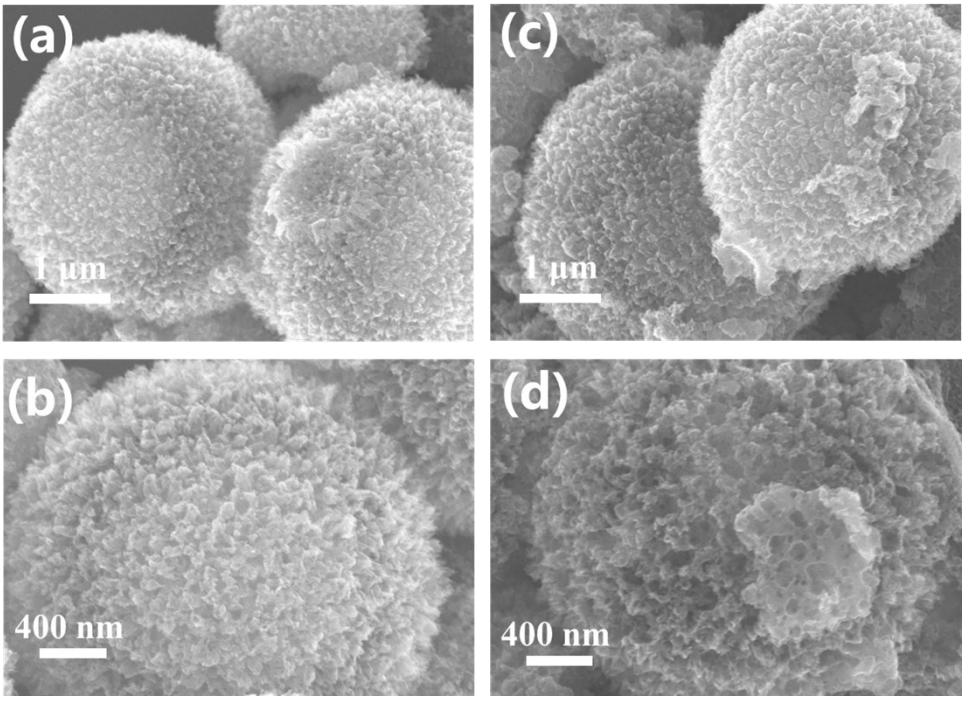

Figure S12. Comparison of (a)(b) before and (c)(d) after CO_2RR at -0.78 V for 1h for Ni@N-HCS-800.

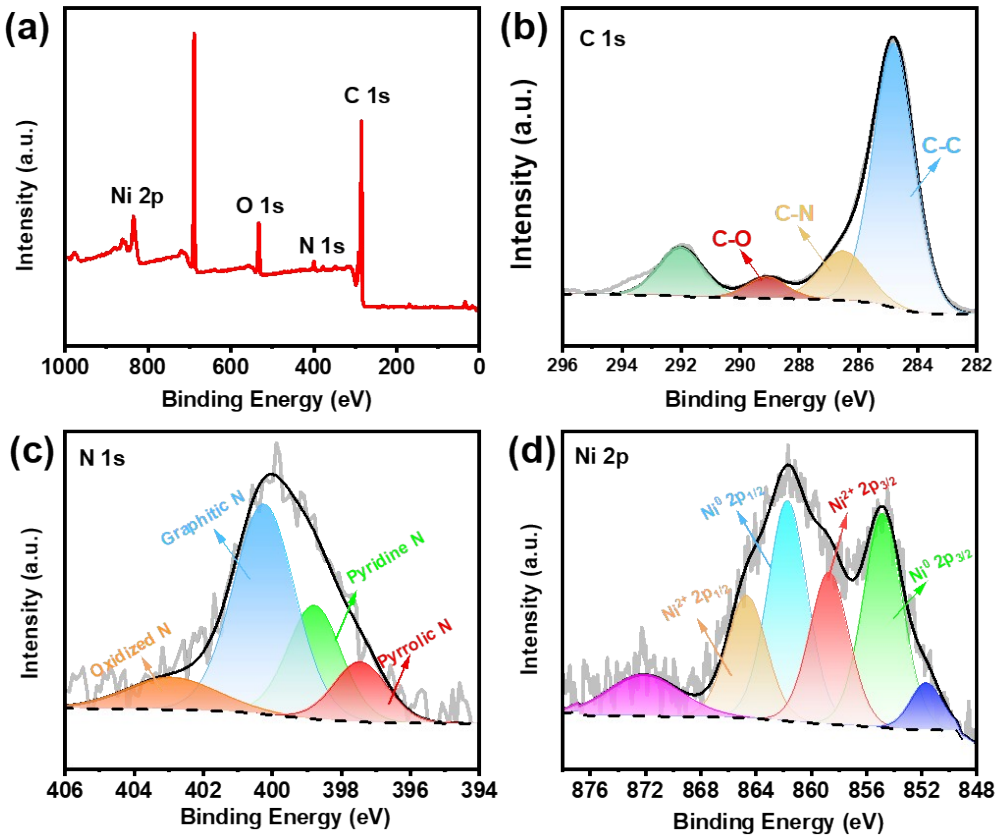

Figure S13. XPS analysis of Ni@N-HCS-800 after CO_2RR at -0.78 V for 1h.

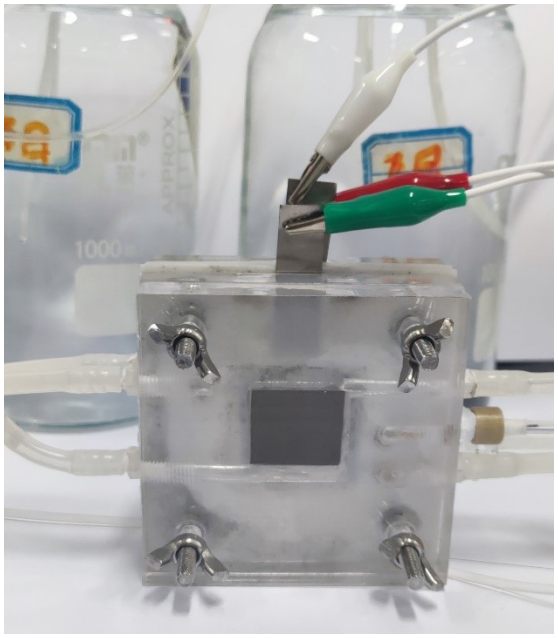

Figure S14. The photograph of Zn-CO_2 flow battery.

Figure S15. Physical picture of the in-situ infrared spectroscopy online device.

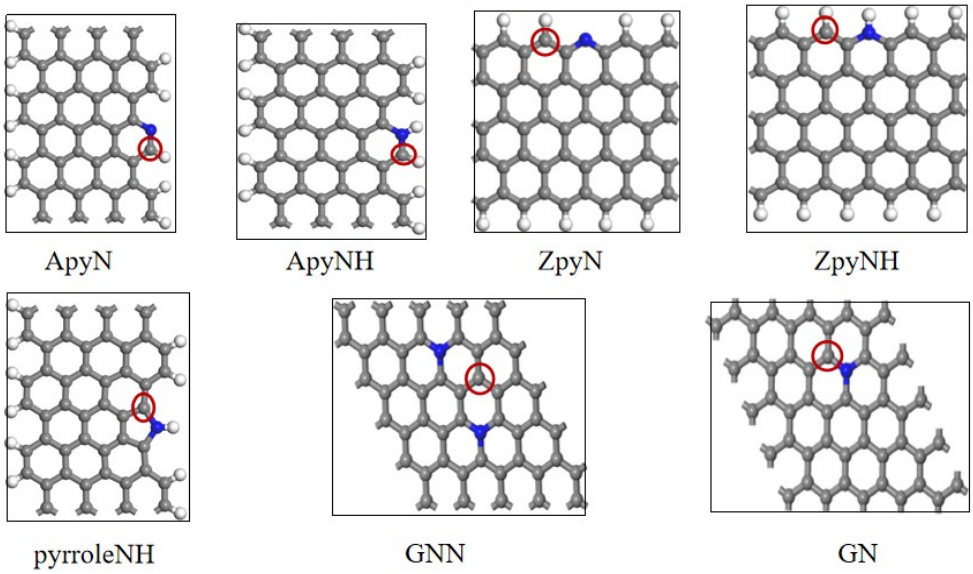

Figure S16. N doped graphene structure; red circle is the active site.

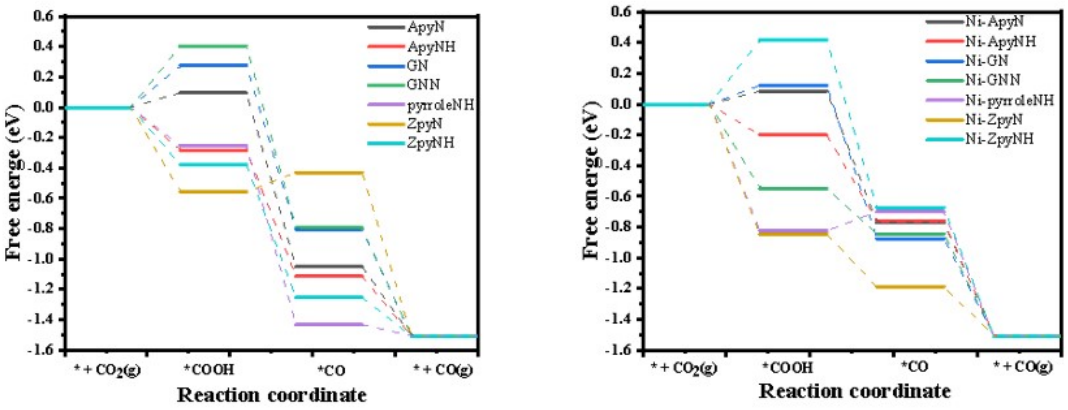

Figure S17. The free energy diagrams (FED) of CO_2RR.

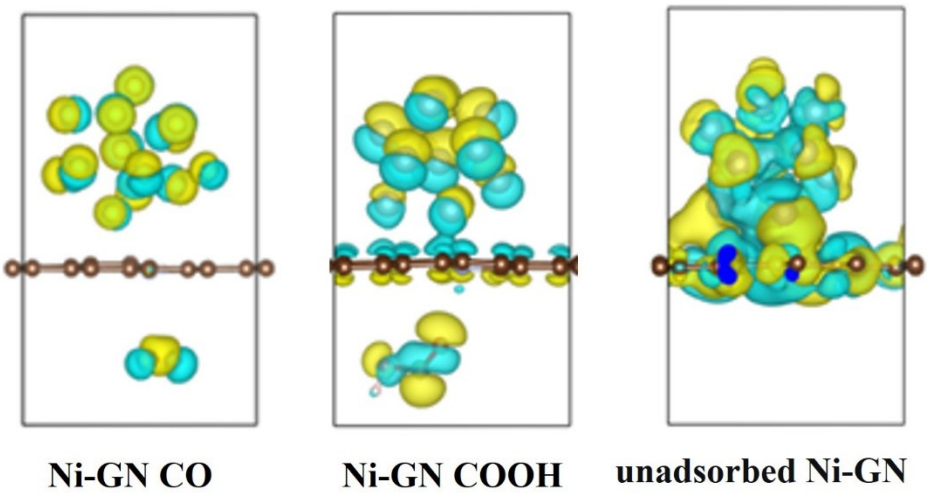

Figure S18. Charge density maps of Ni-GN.

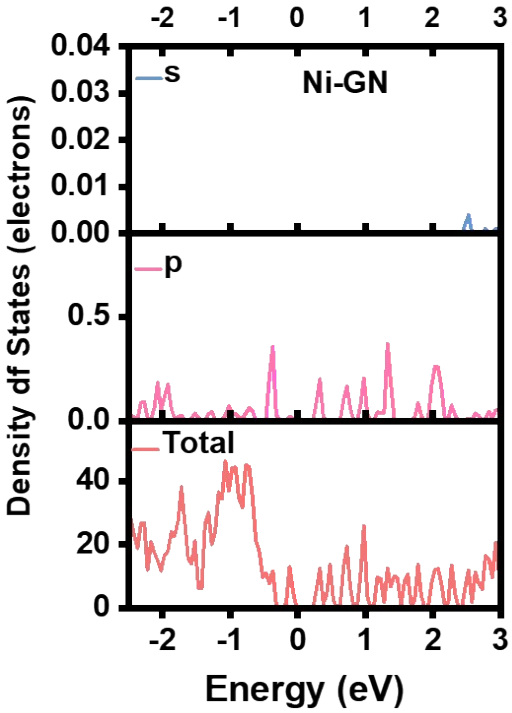

Figure S19. Projected Density of States (PDOS) analysis of Ni-GN.

Table S1. Nitrogen contents in Ni@N-HCS-700, Ni@N-HCS-800 and Ni@N-HCS-900 based on N 1s XPS spectra.

Catalysts	Pyridine-N (%)	Pyrrolic-N (%)	Graphitic-N (%)	Oxidized-N (%)	Pyrrolic-N + Graphitic-N
Ni@N-HCS-700	52.3	11.2	30.6	5.9	41.8
Ni@N-HCS-800	27.1	15.5	48.1	9.3	63.6
Ni@N-HCS-900	20.3	18.8	51.1	9.8	69.9
Ni@N-HCS-800 without acid etch	47.3	-	34.1	18.5	34.1

Table S2. Comparison of the content of each species before and after etching.

Catalysts	Nitrogen (%)	Carbon (%)	Nickel (%)	Nickel oxide (%)
Ni@N-HCS-800	8.89	83.8	7.31	1.97
Ni@N-HCS-800 without acid etch	8.28	85.24	6.48	1.42

Table S3. The E-CO_2RR performance of recently reported catalysts in H-cell.

Catalyst	Electrolyte	Durability/h	Potential /V_{RHE}	J_{CO}/mA cm^{-2}	$FE_{CO(max)}$/ %	Ref.
Ni@N-HCS-800	**0.5 M $KHCO_3$**	12	-0.78	9.58	90.38	**This work**
Ni/HMCS-3-800	0.5 M $KHCO_3$	10	-1.1	10.5	93	[10]
Ni-N-C	0.5 M $KHCO_3$	1.3	-0.7	13	~95	[11]
Ni@N-BPC	0.5 M $KHCO_3$	12	-0.9	~8	98.41	[12]
Ni@NC	0.5 M $KHCO_3$	12	-0.8	23.8	97.8	[13]
Ni@N-C	0.5 M $KHCO_3$	65	-0.8	17	90	[14]

Table S4. Comparison of the performances of Ni@N-HCS-800 catalyst based on the previously reported materials for Zn-CO_2 batteries.

Catalyst	Catholyte	Discharge products	OCP (V)	P_{max} (mW cm^{-2})	Stability	Ref.
Ni@N-HCS-800	1 M $KHCO_3$	CO	1.59	11.55	140 h	**This work**
BiC/HCS	0.8 M $KHCO_3$	HCOOH	0.94	7.2 ± 0.5	65 h	[15]
Bi nanoparticles	0.5 M $KHCO_3$	HCOOH	~1.1	1.43	20 h	[16]
3D Pd IN	0.1 M NaCl	HCOOH	0.89	~6	33 h	[17]
Fe_1NC/S_1	0.5 M $KHCO_3$	CO	0.727	0.6	25 h	[18]
Ni@N-C	1 M $KHCO_3$	CO	–	1.64	45 h	[14]
Cu_3P/C	0.1 M $NaHCO_3$	CO	1.5	2.6	–	[19]
CA/N-Ni	0.5 M $KHCO_3$	CO	–	0.5	30 h	[20]

Table S5. The correction from the zero-point energy, entropy, and heat capacity for converting the total energies to Gibbs free energies (units: eV) [21-25].

Species	ZPE	TS	$\int C_p dT$
COOH*	0.41	0.17	0.09
CO*	0.11	0.08	0.05
H_2	0.27	0.42	0.09
H_2O	0.58	0.42	0.09

References

[1] P. Giannozzi, S. Baroni, N. Bonini, M. Calandra, R. Car, C. Cavazzoni, D. Ceresoli, G.L. Chiarotti, M. Cococcioni, I. Dabo, A. Dal Corso, S. de Gironcoli, S. Fabris, G. Fratesi, R. Gebauer, U. Gerstmann, C. Gougoussis, A. Kokalj, M. Lazzeri, L. Martin-Samos, N. Marzari, F. Mauri, R. Mazzarello, S. Paolini, A. Pasquarello, L. Paulatto, C. Sbraccia, S. Scandolo, G. Sclauzero, A.P. Seitsonen, A. Smogunov, P. Umari, R.M. Wentzcovitch, *J. Phys. Condens. Mat.*, 2009, **21**, 395502.

[2] J.K. Nørskov, J. Rossmeisl, A. Logadottir, L. Lindqvist, J.R. Kitchin, T. Bligaard, H. Jónsson, *J. Phys. Chem. B*, 2004, **108**, 17886-17892.

[3] S. Kozuch, J.M.L. Martin, 2011, **12**, 1413-1418.

[4] K.S. Exner, H. Over, *Acc. Chem. Res.*, 2017, **50**, 1240-1247.

[5] J. Chen, Y. Chen, P. Li, Z. Wen, S. Chen, *ACS Catal.*, 2018, **8**, 10590-10598.

[6] S.S. S. Kozuch, *Acc. Chem. Res.*, 2011, **44**, 101-110.

[7] K. Li, M. Ji, R. Chen, Q. Jiang, J. Xia, H. Li, *Chinese J. Catal.*, 2020, **41**, 1230-1239.

[8] J. K. Nørskov, J. Logadottir, A. Lindqvist, J. R. Kitchin, T. Bligaard, H. JÓnsson, *J. Phys. Chem. B*, 2004, **108**, 17886-17892.

[9] G. Chai, C. Lin, J. Wang, M. Zhang, J. Wei, W. Cheng, *J. Phys. Chem. C.*, 2011, **115**, 2907-2913.

[10] W. Xiong, H. Li, H. Wang, J. Yi, H. You, S. Zhang, Y. Hou, M. Cao, T. Zhang, R. Cao, *Small*, 2020, **16**, 2003943.

[11] J. Wang, Y. Huang, Y. Wang, H. Deng, Y. Shi, D. Wei, M. Li, C. Dong, H. Jin, S. S. Mao, S. Shen, *ACS Catal.*, 2023, **13**, 2374-2385.

[12] S. Zhao, K. Zhang, L. Wu, X. Du, S. Sun, Y. Wang, J. Li, Z. Zhang, *Energy Fuels*, 2024, **38**, 11909-11917.

[13] L. Han, C. Wang, H. Xu, M. Yang, B. Li, M. Liu, *J. Mater. Chem. A*, 2024, **12**, 9462.

[14] F. Wang, G. Wang, P. Deng, Y. Chen, J. Li, D. Wu, Z. Wang, C. Wang, Y. Hua, X. Tian, *Small*, 2023, **19**, 2301128.

[15] M. Yang, S. Liu, J. Sun, M. Jin, R. Fu, S. Zhang, H. Li, Z. Sun, J. Luo, X. Liu, *Appl. Catal. B Environm.*, 2022, **307**, 121145.

[16] Y. Wang, L. Xu, L. Zhan, P. Yang, S. Tang, M. Liu, X. Zhao, Y. Xiong, Z. Chen, Y. Lei, *Nano Energy*, 2022, **92**, 106780.

[17] J. Xie, X. Wang, J. Lv, Y. Huang, M. Wu, Y. Wang, J. Yao, *Angew. Chem. Inter. Ed.*, 2018, **57**, 16996-17001.

[18] T. Wang, X. Sang, W. Zheng, B. Yang, S. Yao, C. Lei, Z. Li, Q. He, J. Lu, L. Lei, L. Dai, Y. Hou, Adv. Mater., 2022, **32**, 2002430.

[19] M. Peng, S. Ci, P. Shao, P. Cai, Z. Wen, *J. Nanosci. Nanotechnol.*, 2019, **19**, 3232-3236.

[20] Y. Zhang, X. Wang, S. Zheng, B. Yang, Z. Li, J. Lu, Q. Zhang, N.M. Adli, L. Lei, G. Wu, Y. Hou, *Adv. Funct. Mater.*, 2021, **31**, 2104377.

[21] L.C. Grabow, M. Mavrikakis, *ACS Catal.*, 2011, **1**, 365-384.

[22] H.A. Hansen, J.B. Varley, A.A. Peterson, J.K. Norskov, *J. Phys. Chem. Lett.*, 2013, **4**, 388-392.

[23] P. Hirunsit, *J. Phys. Chem. C*, 2013, **117**, 8262-8268.

[24] M. Karamad, H.A. Hansen, J. Rossmeisl, J.K. Nørskov, *ACS Catal.*, 2015, **5**, 4075-4081.

[25] M. Liu, Y. Pang, B. Zhang, P. De Luna, O. Voznyy, J. Xu, X. Zheng, C.T. Dinh, F. Fan, C. Cao, F.P. de Arquer, T.S. Safaei, A. Mepham, A. Klinkova, E. Kumacheva, T. Filleter, D. Sinton, S.O. Kelley, E.H. Sargent, *Nature*, 2016, **537**, 382-386.